Chemical and structural characterization of UICC amosite fibres from Penge mine (South Africa)

Paolo Ballirano [1,2], Henrik Skogby [3], Flaminia Gianchiglia [1],
Maria Cristina Di Carlo [1], Antonella Campopiano [4], Annapaola Cannizzaro [4],
Angelo Olori [4], Alessandro Pacella [1,*]

[1] Department of Earth Sciences, Sapienza University of Rome, Piazzale Aldo Moro, 5-I-00185 Roma, Italy
[2] Rectorial Laboratory Fibres and Inorganic Particulate, Sapienza University of Rome, Piazzale Aldo Moro, 5-I-00185 Roma, Italy
[3] Swedish Museum of Natural History, Department of Geosciences, Box 50007, SE-104 05 Stockholm, Sweden
[4] Department of Medicine, Epidemiology, Occupational and Environmental Hygiene, National Institute for Insurance against Accidents at Work (INAIL), Rome, Italy

ARTICLE INFO

ABSTRACT

In the present work we report the full structural and spectroscopic characterization of an UICC amosite (fibrous grunerite) standard sample from Penge mine (South Africa). The chemical composition was obtained by SEM-EDS and cation site partition was retrieved by complementing chemical, Mössbauer and X-ray powder diffraction data. Cell parameters, fractional coordinates, and site scattering for $M(1)$, $M(2)$, $M(3)$, $M(4)$ were refined using the Rietveld method. The retrieved crystal chemical formula $^A[Na_{0.02}]_{\Sigma 0.02}{}^B(Fe^{2+}_{1.54}Mn_{0.29}Na_{0.10}Ca_{0.07})_{\Sigma 2.00}{}^C(Fe^{2+}_{2.92}Mg_{1.93}Fe^{3+}_{0.15})_{\Sigma 5.00}{}^T(Si_{7.93}Al_{0.07})_{\Sigma 8.00}O_{22.00}{}^W(OH_{2.00})_{\Sigma 2.00}$ is in reasonable agreement with reference data.

Rietveld refinement results evidenced that Fe^{2+} is allocated in the octahedral layer following the site preferences $M(1){\approx}M(3){>}M(2)$, whereas Mg preferentially is ordered at $M(2)$. Refined cell parameters are: a=9.55264(17) Å, b=18.3069(3) Å, c=5.33487(8) Å, β=101.840(3)°, V=913.11(3) Å^3. Quantitative Phase Analysis indicates about 10 wt.% of accessory phases including quartz, ankerite and minor stilpnomelane and biotite/annite. Obtained results are the basis for further studies aimed at investigating possible correlation between physico-chemical features of the fibres and their chemical reactivity and toxicity.

Keywords: asbestos; UICC amosite; fibrous grunerite; Scanning Electron Microscopy with Energy Dispersive System (SEM-EDS); Mössbauer Spectroscopy; X-ray Powder Diffraction (XRPD), Rietveld method.

INTRODUCTION

The term asbestos comprises six naturally occurring silicate including chrysotile (serpentine group) and five fibrous amphiboles (anthophyllite, tremolite, actinolite, riebeckite, and grunerite, with the last two commercially known as crocidolite and amosite, respectively).

Due to its electrical and thermal resistance, tensile strength and flexibility, asbestos has been widely attractive to industry for products such as textiles, brakes, cement construction materials and other similar products. Today asbestos use is indeed banned in more than 50 countries (Spasiano and Pirozzi, 2017; International

PM

Ban Asbestos Secretariat, 2019), due to health risks following fibre inhalation (IARC, 2012). In particular, the malignant diseases related to asbestos include lung cancer, mesothelioma, and asbestosis (Huang et al., 2011; Mossman et al., 2011).

It is well recognised that asbestos-induced pathologies are linked to the fibrous morphology (Stanton et al., 1981), the high biopersistence *in vivo* of the fibres (Mossman and Churg, 1998; Kamp and Weitzman, 1999) and the fibre surface chemical reactivity (Fubini, 1993, 1996). Because of this complexity, the mechanisms underlying the asbestos toxicity is still poorly understood. Besides, there is an ongoing debate about the lower carcinogenicity risk associated to serpentine asbestos exposure, presumably due to its higher solubility in the body compared to that of amphiboles (Mossman et al., 2011; Bernstein et al., 2013; Garabrant and Pastula, 2018).

Recent works showed that the amphibole asbestos may undergo structural chemical modifications on its surface when in contact with fluids, possibly resulting in the modulation of the fibre reactivity (Andreozzi et al., 2017; Pacella et al., 2021 a,b; Vigliaturo et al., 2022).

The structure of grunerite (Figure 1) has been reported by Finger (1969) and, recently, by Yong et al. (2019) on prismatic crystals. The presence of texture and disorder effects has rendered very difficult the investigation of the structure of amosite by diffraction techniques. Besides, a sample of amosite studied by electron diffraction and high-resolution electron microscopy showed twinning on (100) leading to stacking disorder accounting for the observed anomalies in its diffraction patterns (Chisholm,

1973; Hutchinson et al., 1975).

Sections perpendicular to [001] of amosite examined by high-resolution TEM revealed two kinds of dislocation with about equal frequency, one is on [001] with Burgers vector **a** and the other on [001] with Burgers vector 1/2**a**+1/2**b** (Whittaker et al., 1981).

Recently, Pollastri et al. (2017) reported for the first time the crystal-structure investigation of UICC (Union for International Cancer Control) amosite by using a multi-analytical approach. As expected, the retrieved crystal structure was similar to that of the grunerite sample of Finger (1969), except for smaller cell parameters and volume due to the lower iron content (Fe/Fe+Mg ratio is 0.78 for sample of Pollastri et al. and is 0.88 for sample of Finger) and shorter $M(1,2,3)$-O bond distances. Moreover, they found both Fe^{2+} and Fe^{3+} atoms at $M(1)$, $M(2)$ and $M(3)$ sites, whereas only Fe^{2+} was hosted in $M(4)$. Mg is disordered over the octahedral layer with a preference for site $M(2)$. Minor Ca and Na have been assigned to the A site.

In the frame of a detailed characterization of the UICC amphibole asbestos standards (Pacella et al., 2019) used by our research group in studies aimed at examining potential correlations between physical-chemical features of the fibres and their chemical reactivity and toxicity, in the present work we report the results of the full structural and spectroscopic characterization of an UICC amosite standard sample from Penge mine (South Africa). Cation site partition was obtained from SEM-EDS chemical data integrated with ^{57}Fe Mössbauer spectroscopy and X-ray powder diffraction data.
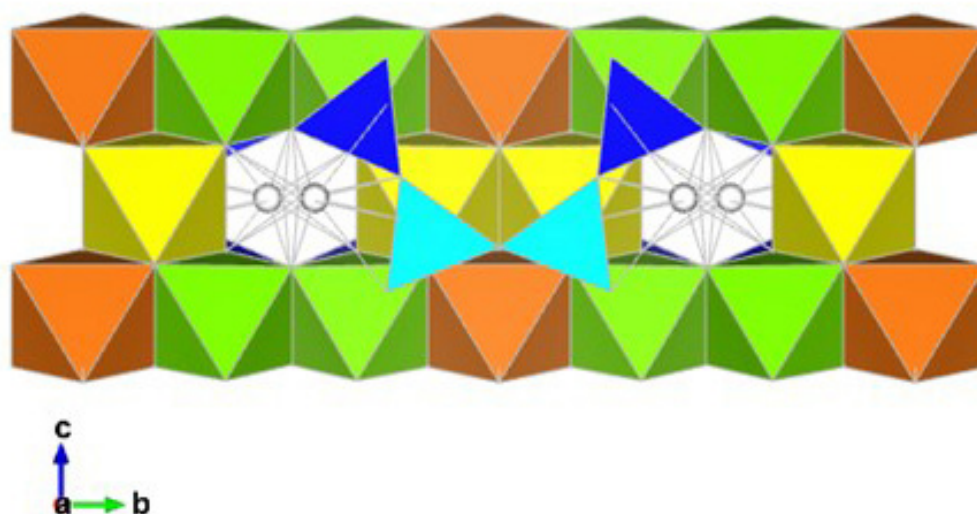

Figure 1. Grunerite structure: projection onto (100) showing the double chain of tetrahedra and the strip of octahedra. Turquoise=T(1), blue =T(2), yellow=$M(1)$, green=$M(2)$, orange=$M(3)$, and white=$M(4)$.

EXPERIMENTAL

Mössbauer spectroscopy

A Mössbauer spectrum of the amosite sample was acquired using a conventional spectrometer system operated in constant-acceleration mode. The Mössbauer absorber was prepared by grinding 50 mg sample material together with ca. 100 mg acrylic resin. The mixture was pressed to a 12 mm diameter disc under mild heating. The spectrum was collected at room temperature using a standard ^{57}Co source in a Rh matrix with a nominal activity of 50 mCi and the absorber placed in 54.7° to the incident beam to avoid texture effects. Spectral acquisition was obtained over 1024 channels in the velocity range -4.2 to + 4.2 mm/s, and the data was then calibrated against a spectrum of an α-Fe foil before folding and fitting using the software MossA (Prescher et al., 2012). The spectrum was treated by using one quadrupole doublet assigned to Fe^{3+} and two doublets assigned to Fe^{2+}, applying Lorentzian line shapes and equal intensities of the quadrupole components. ^{57}Fe Mössbauer parameters for the amosite sample are reported in Table 1.

Scanning Electron Microscopy with Energy Dispersive System (SEM-EDS)

The micro-chemical data were collected on a Quanta 400 SEM (FEI, Hillsboro, Oregon, USA) fitted with an EDX Genesis EDS system and operating at the following conditions: 15 kV accelerating voltage, 11 mm working distance, 0° tilt angle. Analytical points were selected on flattened area of fibre bundles (7 analytical points) to extract quantitative EDS data (Paoletti et al., 2008, 2011; Newbury and Ritchie, 2013; Pacella et al., 2016). Table 2 reports the average chemical composition, expressed as oxides, and the corresponding empirical formula of UICC amosite. The chemical composition was normalized to 100% after Fe^{3+}/Fe^{2+} partition, based on Fe^{3+}/Fe_{tot} of 3.3 % from Mössbauer data, and fixing the H_2O content to stoichiometry (2 OH per formula unit, pfu). The empirical formula was calculated based on 24 O. Cations are reported in atoms per formula unit (apfu) and were assigned to the various T, C and B sites following Hawthorne et

al. (2012). For comparison purposes, reference data of UICC amosite standard (Koyama et al., 1996; Bowes and Farrow, 1997; Pollastri et al., 2017) and of grunerite samples from the Penge area (Miyano and Beukes, 1997) and Moose Mountain Mine, Ontario, Canada (Yong et al., 2019) are also reported.

X-ray Powder Diffraction (XRPD)

X-ray powder diffraction data were measured using a D8 Advance automated powder diffractometer (Bruker AXS, Karlsruhe, Germany) running in θ/θ transmission mode. The sample was gently ground in an agate mortar under ethanol and the resulting powder was loaded in a 0.5 mm diameter borosilicate glass capillary. The instrument is fitted with an incident beam focussing graded multilayer Göbel mirror and a PSD VÅntec-1. The diffraction pattern was collected in step-scan mode, using CuKα, in the 5-145° 2θ angular range, 0.022° 2θ step size and 20 s counting time. Data were evaluated by the Rietveld method using Topas V6 (Bruker AXS, 2016) which implements the Fundamental Parameters Approach FPA (Cheary and Coelho, 1992). Preliminary scrutiny of the pattern indicated the occurrence of a few phases at the minor/trace level. Quartz, ankerite and garnet, owing to their simple structures, were included to the Rietveld refinement. Moreover, only the strong, low-angle reflection of stilpnomelane and biotite/annite was observed. Stilpnomelane (Guggenheim and Eggleton, 1994), a phyllosilicate phase with modulated layers (Dana 74.1.1.1) of ideal formula $(K,Ca,Na)(Fe^{2+},Fe^{3+},Mg,Al)_8$ $(Si,Al)_{12}(O,OH)_{36}\cdot nH2O$, has been reported as an accessory phase in the Penge iron formation, commonly associated to grunerite (Miyano and Beukes, 1997). It is worth noting that the relevant reflection of stilpnomelane (ca. 7.25° 2θ) and biotite/annite (ca. 8.45° 2θ) can be observed also in the original diffraction pattern reported in Figure 2 by Kohyama et al. (1996) for an UICC amosite sample. Only scale factors, cell parameters and peak shapes were refined for quartz, ankerite and garnet. Differently, the main reflection of stilpnomelane and biotite/annite were approximated by two peaks not related to any

Table 1. ^{57}Fe Mössbauer parameters for the amosite sample obtained at room-temperature.

IS (mm/s)	QS (mm/s)	FWHM	Area (%)	Fe_{corr} (%)*	Assignment	apfu
1.153(1)	2.781(2)	0.253(2)	64.6(5)	65.1(5)	Fe^{2+} [M(1),M(2),M(3)]	3.00(2)
1.078(1)	1.572(3)	0.251(5)	31.3(4)	31.6(4)	Fe^{2+} M(4)	1.46(2)
0.36(2)	0.90(4)	0.38(7)	4.1(5)	3.3(5)	Fe^{3+} [M(1),M(2),M(3)]	0.15(2)

*Fe distribution after correction for different recoil-free fractions for Fe^{2+} and Fe^{3+} according to Dyar et al. (1993).

PM

Table 2. Chemical composition and site partition of the UICC amosite sample. Standard deviations (when available) are reported between parentheses. For comparison purposes data of Koyama et al. (1996) (K96), Bowes and Farrow (1997) (BF97) and Pollastri et al. (2017) (P17) for UICC amosite samples and those of Miyano and Beukes (1997) (MB97) for grunerite samples from Penge iron formation, South Africa, and Yong et al. (2019) (Y19) for a grunerite sample from Moose Mountain Mine, Ontario, Canada are also reported.
* Including 1.55 wt% CO_2 arising from admixed carbonates, ** from stoichiometry.
Fe^{3+}/Fe^{2+} partition by gravimetric/colorimetric (K96), titration (BF97 and MB97) and Mössbauer spectroscopy (P17 and present work).

|	Present work	K96	BF97	P17	MB97 PE13 - 29	MB97 PE13 - 111	Y19
SiO_2	50.84 (0.41)	50.63	49.51	49.8 (0.2)	50.94	49.02	49.58
TiO_2	-	-	0.40	0.04 (0.02)	0.05	0.07	0.02
Al_2O_3	0.40 (0.11)	0.55	0.00	0.04 (0.02)	0.03	2.49	0.44
Cr_2O_3	-	-	-	0.01 (0.01)	0.03	-	0.01
Fe_2O_3	1.30 (0.09)	1.90	2.83	3.9 (0.4)	0.30	3.25	-
FeO	34.23 (1.08)	35.41	33.86	37.8 (0.4)	37.74	31.77	39.14
MnO	2.19 (0.17)	1.82	1.80	0.42 (0.6)	0.74	1.15	0.38
NiO	-	-	-	0.02 (0.04)	0.02	-	-
MgO	8.29 (0.61)	6.44	6.76	6.23 (0.9)	8.22	8.40	6.90
CaO	0.44 (0.30)	0.51	0.39	0.09 (0.01)	0.10	2.19	0.36
Na_2O	0.38 (0.26)	0.02	0.12	0.03 (0.02)	0.02	0.38	0.05
K_2O	-	0.27	0.13	0.02 (0.01)	0.00	0.15	0.01
H_2O	1.92**	2.32	2.72	1.94 (0.00)	1.92**	1.94**	1.88**
total	100.00	99.87	100.08*	100.32	100.11	100.81	98.77
				T			
Si	7.93	7.91	7.80	7.86	7.97	7.56	7.93
Al	0.07	0.09	-	0.01	0.01	0.44	0.07
Σ	8.00	8.00	7.80	7.87	7.98	8.00	8.00
				C			
Fe^{2+}	2.92	3.03	2.78	3.00	2.93	2.52	3.34
Mg	1.93	1.50	1.59	1.47	1.92	1.93	1.65
Fe^{3+}	0.15	0.22	0.34	0.46	0.04	0.38	-
Mn	-	0.24	0.24	0.06	0.10	0.15	-
Al	-	0.01	-	-	-	0.01	0.01
Ti	-	-	0.05	-	0.01	0.01	-
Σ	5.00	5.00	5.00	4.99	5.00	5.00	5.00
				B			
Fe^{2+}	1.54	1.60	1.68	2.00	2.00	1.58	1.90
Mn	0.29	-	-	-	-	-	0.05
Na	0.10	0.01	0.04	-	-	0.06	-
Ca	0.07	0.09	0.07	-	-	0.36	0.05
Σ	2.00	1.70	1.79	2.00	2.00	2.00	2.00
				A			
Na	0.02	-	-	0.01	0.01	0.06	0.02
Ca	-	-	-	0.02	0.02	-	0.01
K	-	0.05	0.03	-	-	0.03	-
Σ	0.02	0.05	0.03	0.03	0.03	0.09	0.03
O	22.00	21.58	21.18	21.96	22.00	22.00	22.00
OH	2.00	2.42	2.86	2.04	2.00	2.00	2.00
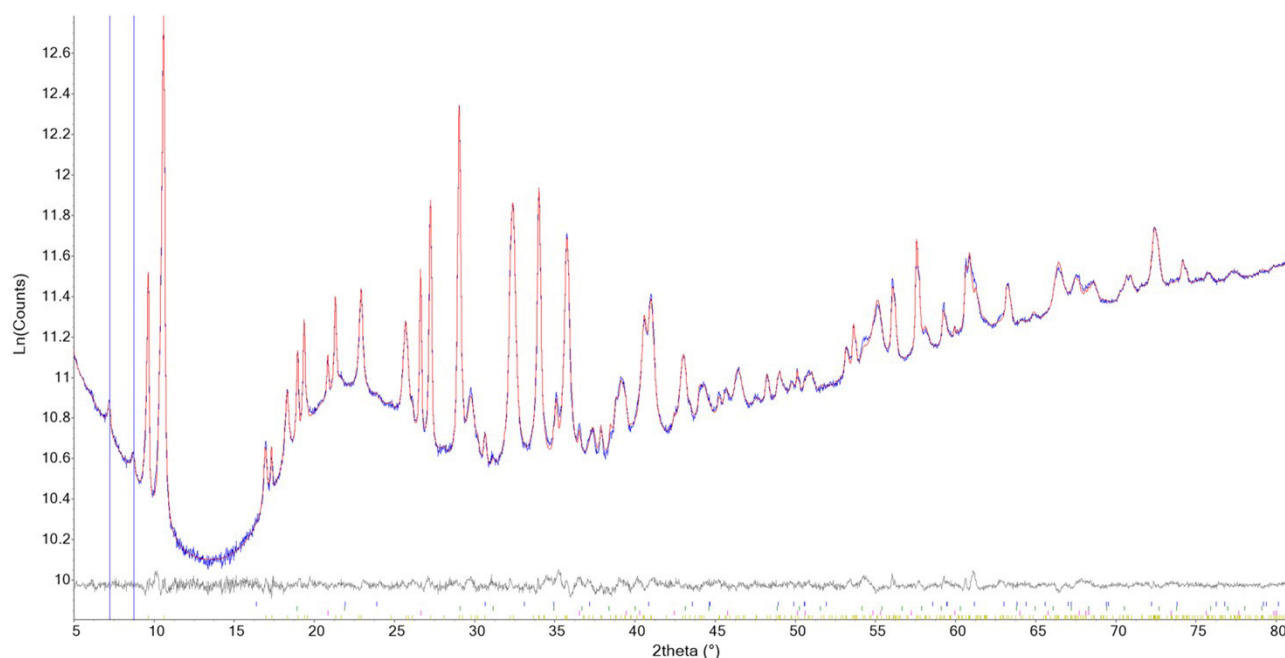
Figure 2. Magnified view (5-80° 2θ) of the Rietveld plots of the refinement of the UICC amosite sample. Intensity scale logarithmic. Blue: experimental; red: calculated; grey: difference; vertical bars indicate the position of the calculated Bragg reflections of (from above to below) ankerite (blue), garnet (green), quartz (magenta) and amosite (yellow).
The vertical blue lines indicate the position of the main reflection of stilpnomelane (7.25° 2θ) and biotite/annite (8.45° 2θ), respectively, that were approximated by peaks unrelated to structures.

structure whose position, intensity and breadth were also refined following the same procedure applied by Pacella et al. (2021 a,b). However, this simplified approach does not allow quantification of the two phases that, based on the intensity and breadth of the two reflections, may be estimated at the 2-3 wt% level.

Following a well-established procedure, the structure of amosite was refined keeping all displacement parameters fixed to reference data (grunerite of similar chemical composition: Yong et al., 2019) and no restraints on bond distances and angles were imposed. Site scattering (*s.s.*) at $M(1)$, $M(2)$, $M(3)$ and $M(4)$ was optimized. Moreover, due to the presence of 0.29 apfu Mn we attempted, without success, to add a split $M(4')$ site to the refinement following the finding of Oberti et al. (2006). No electron density was detected at A-type sites in agreement with the micro-chemical data.

The refinement was started using a conventional description of the peak broadening characterized by a Lorentzian (size) and a Gaussian (strain) behaviour (Delhez et al., 1993). However, a significant and complex anisotropic broadening of the diffraction maxima was observed that was initially modelled using the ellipsoid-model of Katerinopoulou et al. (2012). However, the application of normalized symmetrized spherical harmonics functions, described by Järvinen

(1993), produced a further, significant, improvement of the fit. The absorption effects were modelled using the equation of Sabine et al. (1998) for a cylindrical sample and the presence of preferred orientation was corrected using normalized symmetrized spherical harmonics functions. The number of terms (4th-order, eight refinable parameters) was chosen in keeping with the procedure of Ballirano (2003). Parameters refined to small values as expected for a sample prepared as capillary.

The Quantitative Phase Analysis (QPA) is shown in Table 3, the list of the starting structural data is reported in Table 4 and the statistical indicators of the refinement are listed in Table 5. A magnified view (5-80° 2θ) of the Rietveld plots is shown in Figure 2. QPA follows the check list indicated in Gualtieri et al. (2019). The CIF file of UICC amosite is deposited as supporting material at the journal's site.

RESULTS AND DISCUSSION

The [57]Fe Mössbauer spectrum of the amosite sample (Figure 3) shows two well-separated doublets with relatively large quadrupole splitting and a fairly weak shoulder feature around 0.8 mm/s. The spectrum could be accurately fitted with two Fe^{2+} doublets and one Fe^{3+} doublet. In line with previous Mössbauer studies of amosite and grunerite spectra (e.g. Bancroft et al., 1967;

Table 3. Quantitative phase analysis (QPA) of the UICC amosite sample. Reference data of Koyama et al. (1996) (K96) and Pollastri et al. (2017) for UICC amosite (P17) are reported for comparison.

* Re-evaluation of the original X-ray diffraction data (reported in Figure 2) indicates the occurrence of traces of both phases.

Phases (wt%)	Present work	K96	P17
Amosite	94.87(8)	99	> 95
Quartz	3.79(5)	< 1	< 1
Ankerite	0.76(4)	-	-
Garnet	0.58(4)	-	-
Stilpnomelane	Traces	-*	-
Biotite/annite	Traces	-*	-
Calcite	-	-	< 1
Hematite	-	-	< 1

Table 4. List of reference starting structural data.

Phases	Reference
Amosite	Yong et al. (2019)
Quartz	Le Page and Donnay (1976)
Ankerite	Ross and Reeder (1992)
Garnet	Sawada (1999)
Stilpnomelane	none - peak phase
Biotite/annite	none - peak phase

Table 5. Statistical indicators of the Rietveld refinement, as defined in Young (1993).

R_{Bragg} (%)	0.58
R_{wp} (%)	1.40
R_p (%)	0.84
GoF	4.08
DWd	0.78

Pollastri et al. 2015), the outer Fe^{2+} doublet is assigned to $M(1)$, $M(2)$, $M(3)$, the inner one to $M(4)$, and the Fe^{3+} doublet to $M(1)$, $M(2)$, $M(3)$. The area ratio for the doublet assigned to Fe^{3+} corresponds to 4.1%. However, according to the study of Dyar et al. (1993), the Mössbauer recoil-free fractions for Fe^{2+} and Fe^{3+} in amphibole are unequal. Following the correction procedure described in Dyar et al. (1993), an Fe^{3+}/Fe_{tot} ratio of 3.3% was obtained.

The SEM-EDS analyses indicate a good chemical homogeneity of the fibres (Table 2) with some minor Mg

vs Fe^{2+} variability. The corresponding empirical formula is:

$$^A[Na_{0.02}]_{\Sigma 0.02}{}^B(Fe^{2+}_{1.54}Mn_{0.29}Na_{0.10}Ca_{0.07})_{\Sigma 2.00}$$
$$^C(Fe^{2+}_{2.92}Mg_{1.93}Fe^{3+}_{0.15})_{\Sigma 5.00}{}^T(Si_{7.93}Al_{0.07})_{\Sigma 8.00}$$
$$O_{22.00}{}^W(OH_{2.00})_{\Sigma 2.00}$$
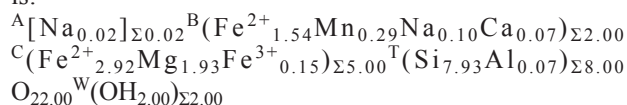
and is in reasonable agreement with those recalculated from the original data of the three UICC amosite standard samples characterized by Koyama et al. (1996)

$$^A(K_{0.05})_{\Sigma 0.05}{}^B(Fe^{2+}_{1.60}Na_{0.01}Ca_{0.09})_{\Sigma 1.70}{}^C(Fe^{2+}_{3.03}Mg_{1.50}$$
$$Mn_{0.24}Fe^{3+}_{0.22}Al_{0.01})_{\Sigma 5.00}{}^T(Si_{7.91}Al_{0.09})_{\Sigma 8.00}$$
$$O_{21.58}{}^W(OH_{2.32})_{\Sigma 2.42},$$

Bowes and Farrow (1997)$^A(K_{0.03})_{\Sigma 0.03}{}^B(Fe^{2+}_{1.68}$ $Ca_{0.07}Na_{0.04})_{\Sigma 1.79}{}^C(Fe^{2+}_{2.78}Mg_{1.59}Fe^{3+}_{0.34}$ $Mn_{0.24}Ti_{0.05})_{\Sigma 5.00}$ $^T(Si_{7.80})_{\Sigma 7.80}O_{21.18}{}^W(OH_{2.86})_{\Sigma 2.86}$
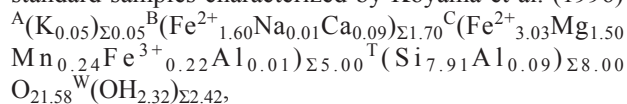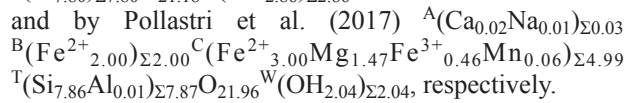
and by Pollastri et al. (2017) $^A(Ca_{0.02}Na_{0.01})_{\Sigma 0.03}$ $^B(Fe^{2+}_{2.00})_{\Sigma 2.00}{}^C(Fe^{2+}_{3.00}Mg_{1.47}Fe^{3+}_{0.46}Mn_{0.06})_{\Sigma 4.99}$ $^T(Si_{7.86}Al_{0.01})_{\Sigma 7.87}O_{21.96}{}^W(OH_{2.04})_{\Sigma 2.04}$, respectively.

As previously pointed out for the UICC crocidolite standard (Pacella et al., 2019), some chemical variability exists among various batches and this behaviour is coherent with the variability typically observed at the Penge iron formation. As an example, we report the chemical composition of two samples of grunerite retrieved from a diamond drill core at different depths (PE13-29 and PE13-111) and reported by Miyano and Beukes (1997). It is worth noting that the apfu Fe^{2+} assigned to C and B group sites (Table 1) from Mössbauer data are in very good agreement with the empirical formula calculated from SEM-EDS analysis. Moreover, the large Mn content (2.2 wt% as MnO) is comparable with the value of 1.8 wt% detected in UICC amosite sample by Kohyama et al. (1996).

Cell parameters and volume of UICC amosite are a=9.55264(17) Å, b=18.3069(3) Å, c=5.33487(8) Å, β=101.840(3)°, V=913.11(3) Å^3. They fit nicely into the graphs correlating lattice parameters and Fe/(Fe+Mg) content for natural and heated "cummingtonites" reported in Figure 1 by Hirschmann et al. (1994). In Table 6 the present cell parameters are compared to those of Pollastri et al. (2017) for the UICC amosite standard and to those of Yong et al. (2019) for a grunerite crystal of analogous chemical composition. As can be seen, values are similar and reflect the observed minor chemical differences among the samples (Table 6). The QPA testify some heterogeneity of the UICC amosite standard similarly to UICC crocidolite standard (Pacella et al., 2019) as the identified minor/trace phases differ both in terms of species and quantity. In fact, the present sample shows a significantly higher quartz content as compared to reference data (Table 4) and the estimated amosite content should be possibly at a lower degree of purity (>90 wt% level) with respect to the batches analysed by Kohyama et al. (1996) and Pollastri et al. (2017). Relevant bond distances of UICC amosite are
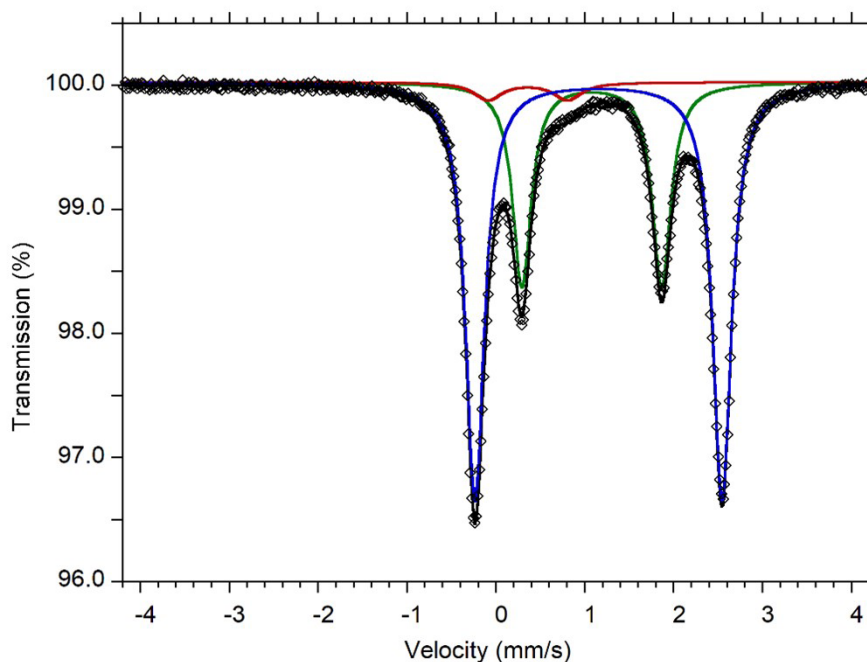
Figure 3. ^{57}Fe Mössbauer spectrum of amosite obtained at room-temperature. Fitted absorption doublets assigned to Fe^{2+} in $M(1)$, $M(2)$, $M(3)$ are indicated in blue, Fe^{2+} in $M(4)$ in green, and Fe^{3+} in red. Diamonds denote measured spectrum, and black curve represents summed fitted spectrum.

Table 6. Cell parameters and volume of the UICC amosite sample. Reference data of Pollastri et al. (2017) for UICC amosite (P17) and of Yong et al. (2019) for grunerite (Y19) are reported for comparison.

	Present work	P17	Y19
a (Å)	9.55264(17)	9.5482(2)	9.5534(11)
b (Å)	18.3069(3)	18.3395(4)	18.328(2)
c (Å)	5.33487(8)	5.3346(1)	5.3382(8)
b (°)	101.840(3)	101.825(2)	101.854(4)
V (Å^3)	913.11(3)	914.31(3)	914.7(2)

reported in Table 7, where they are compared to those of Pollastri et al. (2017) and Yong et al. (2019). The $<T(1)–O>$ and $<T(2)–O>$ observed in the present refinement are identical whereas in amphiboles, in the absence of Al, $<T(2)–O>$ is slightly longer. This fact suggests, in agreement with reference data, that 0.07 apfu Al are allocated at $T(1)$ (Oberti et al., 2007). In general, structural data of the present refinement are in close agreement with those of the grunerite sample of Yong et al. (2019). In fact, the $<<M(1), M(2), M(3)–O>>$ is of 2.114 Å as compared to 2.117 Å of Yong et al. (2019) reflecting the higher Fe^{2+} content at C group sites of the grunerite sample (3.34

apfu) with respect to the present UICC amosite standard (2.92 apfu). UICC amosite shows a slightly more regular octahedral coordination for $M(1)$ with respect to the grunerite sample of Yong et al. (2019). Some differences are observed with respect to the $M–O$ bond distances reported by Pollastri et al. (2017) that are systematically shorter than those obtained in both the present and in the grunerite refinement despite an intermediate Fe^{2+} content at C group sites. The same shortening has been observed for $<M(4)–O>$. The refined $s.s.$ at C group sites [102.8(7) e$^-$] is in remarkable agreement with 103.1 e$^-$ from micro-chemical data, as reported in Table 8. A plot of the $s.s.$ at C group sites obtained by Rietveld refinements, performed on data collected in transmission mode by our research group, and the $s.s.$ at C group sites determined by micro-chemical analyses is reported in Figure 4. The thick black bisecting line is a guide for eyes indicating the ideal behaviour. This graph represents an extension toward compositions enriched in Fe(+Mn) with respect to that proposed by Ballirano et al. (2017) for tremolites. For values of $s.s.$ <80 e$^-$ it was observed a linear dependence with a progressive increase of the misfit between the $s.s.$ from micro-chemical data and that from Rietveld refinements with increasing values of $s.s.$ (Vignaroli et al., 2014; Ballirano et al., 2017). However, both UICC amosite and UICC crocidolite samples show a remarkable agreement between

Table 7. Relevant bond distances (Å) of UICC amosite. Reference data of Pollastri et al. (2017) for UICC amosite (P17) and of Yong et al. (2019) for grunerite (Y19) are reported for comparison.
* Calculated as in Table 7 of Hawthorne and Oberti (2007).

		Present work	P17	Y19
$T(1)$	–O1	1.631(12)	1.629(6)	1.617(2)
	–O5	1.615(12)	1.610(5)	1.6524(2)
	–O6	1.650(10)	1.622(6)	1.622(2)
	–O7	1.606(5)	1.651(5)	1.6196(13)
$<T(1)–O>$		1.626	1.628	1.621
$T(2)$	–O2	1.621(12)	1.649(5)	1.625(2)
	–O4	1.609(9)	1.639(5)	1.607(2)
	–O5	1.615(10)	1.633(5)	1.632(2)
	–O6	1.659(11)	1.635(6)	1.653(2)
$<T(2)–O>$		1.626	1.633	1.629
$M(1)$	–O1 x2	2.079(12)	2.079(9)	2.085(2)
	–O2 x2	2.133(9)	2.087(9)	2.163(2)
	–O3 x2	2.132(9)	2.091(9)	2.116(2)
$<M1–O>$		2.115	2.088	2.121
$<r_{M(1)}>$		0.755	0.728	0.761
$M(2)$	–O1 x2	2.155(9)	2.09(1)	2.162(2)
	–O2 x2	2.112(12)	2.09(1)	2.116(2)
	–O4 x2	2.064(8)	2.072(9)	2.068(2)
$<M(2)–O>$		2.110	2.084	2.115
$<r_{M(2)}>$		0.750	0.724	0.755
$M(3)$	–O1 x4	2.121(9)	2.082(9)	2.127(2)
	–O3 x2	2.111(15)	2.080(8)	2.087(3)
$<M(3)–O>$		2.118	2.081	2.114
$<r_{M(3)}>$		0.758	0.721	0.754
$<<M(1),M(2),M(3)–O>>$		2.114	2.084	2.117
$<r_{M(1),(2),(3)}>$		0.754	0.724	0.757
$<<r^{M(1,2,3)}>>$*		0.767	0.729	0.770
$M(4)$	–O2 x2	2.189(9)	2.087(9)	2.139(2)
	–O4 x2	1.997(10)	2.06(1)	1.989(2)
	–O6 x2	2.749(10)	2.54(1)	2.736(3)
$<M(4)–O>$		2.312	2.233	2.288

s.s. from micro-chemical data and Rietveld refinement, possibly suggesting a reversal of the behaviour starting for composition having *s.s.* >80 e⁻. A tentative third-order polynomial fit has been superimposed to the data. Some additional data for intermediate compositions are required to model in a more accurate way this behaviour. This systematic misfit has not yet been explained except for a possible imperfect absorption correction (Ballirano et al., 2017). Cation partition is reported in Table 8 hypothesizing that all Mn is allocated at $M(4)$. The C group sites preference of ferrous iron is $M(1)»M(3)>M(2)$ with Mg preferentially ordered at $M(2)$ in agreement with reference data (Hirschmann et al., 1994). Following the approach first introduced by Vignaroli et al. (2014) and subsequently successfully adopted for several structural characterizations of fibrous amphiboles, an indirect Fe^{2+}/Fe^{3+} partition was attempted by comparing the $<r_M>$ mean cationic radii calculated from both the refined $<M(1,2,3)–O>$ bond distances and from the proposed site partition (Table 9). Results suggest a unusual preferential

Table 8. Site scattering (*s.s.* in e⁻) and cation partition of the UICC amosite sample. Reference data of Pollastri et al. (2017) for UICC amosite (P17) and of Yong et al. (2019) for grunerite (Y19) are reported for comparison.
[§] plus additional 0.06 apfu Mn; [#] plus additional 0.01 apfu Al.

Site	*s.s.*	partition from *s.s.*	partition from SEM/EDS	P17 partition from *s.s.*	P17 partition from EMPA	Y19 partition from *s.s.*	Y19 partition from EMPA
C							
$M(1)$	43.5(3)	$Mg_{0.60}Fe_{1.40}$		$Mg_{0.20}Fe_{1.80}$		$Mg_{0.54}Fe_{1.46}$	
$M(2)$	37.2(2)	$Mg_{1.05}Fe_{0.95}$		$Mg_{0.64}Fe_{1.36}$		$Mg_{0.88}Fe_{1.12}$	
$M(3)$	22.0(2)	$Mg_{0.29}Fe_{0.71}$		$Mg_{0.13}Fe_{0.87}$		$Mg_{0.25}Fe_{0.75}$	
		$\Sigma Mg_{1.94}Fe_{3.06}$	$\Sigma Mg_{1.92}Fe_{3.08}$	$\Sigma Mg_{0.97}Fe_{4.03}$	$[§]\Sigma Mg_{1.47}Fe_{3.46}$	$\Sigma Mg_{1.67}Fe_{3.33}$	$[#]\Sigma Mg_{1.65}Fe_{3.34}$
Total		102.8(7)	103.1	116.5(13)	109.1	106.6(5)	106.8
B							
$M(4)$		$Fe_{1.59}Mn_{0.29}Ca_{0.12}$	$Fe_{1.54}Mn_{0.29}Na_{0.10}Ca_{0.07}$	$Fe_{2.00}$	$Fe_{2.00}$	$Fe_{1.93}Ca_{0.04}$	$Fe_{1.90}Mn_{0.05}Ca_{0.05}$
Total		51.0(3)	49.8	52	52	51.1(4)	49.8
A		-	$Na_{0.02}$	$Na_{0.01}Ca_{0.02}$	$Na_{0.01}Ca_{0.02}$	-	$Na_{0.02}Ca_{0.01}$

$$y = -0.002 x^2 + 1.345 x - 12.175$$
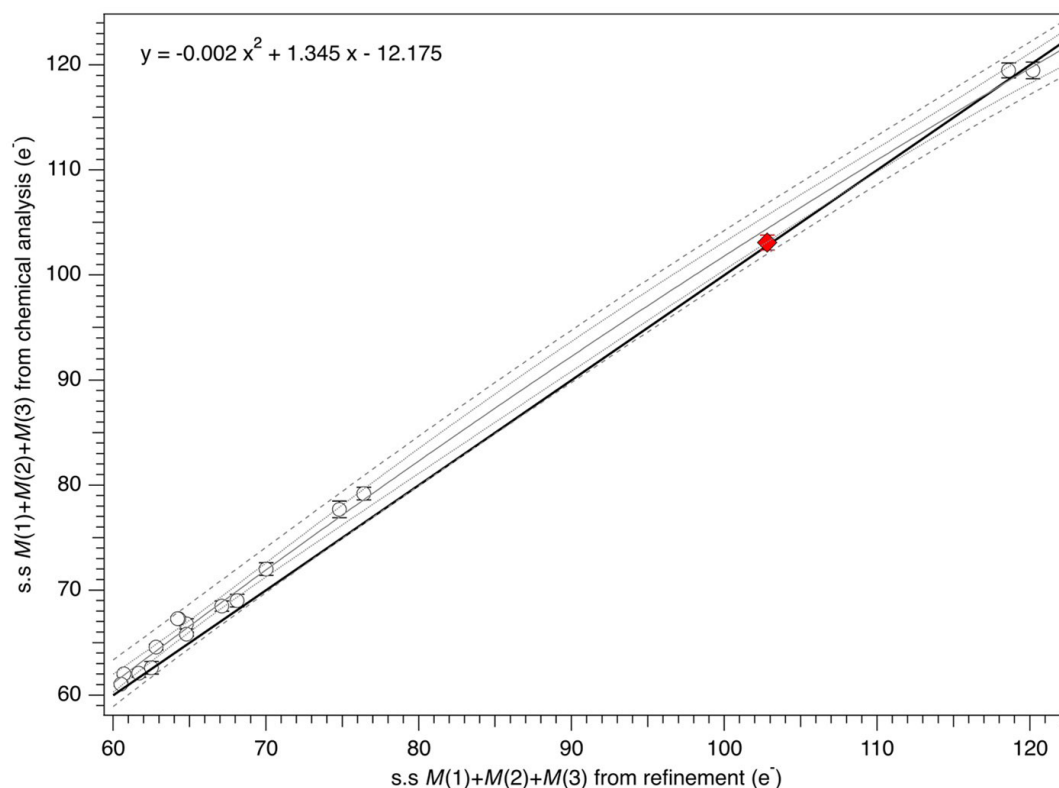
Figure 4. Comparison between the s.s. at C sites obtained by Rietveld refinements performed on data collected in transmission mode and the *s.s.* at C sites determined by micro-chemical analyses. UICC amosite indicated as a red diamond. Linear regression, confidence (95% level), and prediction intervals are reported as full, short dash, and dotted lines, respectively. Reference data are: Ballirano et al. (2008); Pacella et al. (2008); Andreozzi et al. (2009); Vignaroli et al. (2014); Pacella et al. (2019); Pacella et al. (2021a); Ballirano et al. (2021).

Table 9. Fe speciation, following Vignaroli et al. (2014), at the C sites of the UICC amosite sample.

Site	partition from *s.s.*	partition from SEM/EDS and Mössbauer	$<r_M>$ from partition (Å)	$<r_M>$ from refinement (Å)
$M(1)$	$Mg_{0.60}Fe^{3+}_{0.11}Fe^{2+}_{1.29}$		0.755	0.755
$M(2)$	$Mg_{1.05}Fe^{2+}_{0.95}$		0.748	0.750
$M(3)$	$Mg_{0.29}Fe^{3+}_{0.04}Fe^{2+}_{0.67}$		0.758	0.758
	$\Sigma Mg_{1.94}Fe^{3+}_{0.15}Fe^{2+}_{2.91}$	$\Sigma Mg_{1.92}Fe^{3+}_{0.15}Fe^{2+}_{2.93}$		

allocation of Fe^{3+} at $M(1)$ (0.11 apfu) and $M(3)$ (0.04) which is supported only in the case of the simultaneous corresponding presence of an oxo component (Oberti et al., 2007). It should be noted that the total of 0.15 apfu Fe^{3+} is in perfect agreement with that observed from Fe^{3+}/Fe^{2+} partition based on Mössbauer data.

CONCLUSIONS

This work reports an accurate crystal-chemical characterization of the UICC amosite standard sample coming from Penge mine, South Africa, obtained by a multi-analytical approach. Our QPA revealed the occurrence of non-negligible contents of impurities (ca. 10 wt.%) in the hand sample, much more than those observed by Kohyama et al. (1986) and Pollastri et al. (2017). The quantification and identification of these phases is relevant for the correct interpretation of the reactivity studies on this sample.

Since the primary role of iron in Reactive Oxygen Species production (Fubini, 1993, 1996), particular attention has been focused on its position within the mineral structure. Rietveld refinement results evidenced that Fe^{2+} is allocated in the octahedral layer following the site preferences $M(1) \approx M(3) > M(2)$ with Mg preferentially ordered at $M(2)$ in agreement with reference data. In addition, the sample showed a large Mn content that is allocated at $M(4)$ site in agreement with reference data. Mössbauer data indicate a smaller Fe^{3+}/Fe_{tot} ratio (3.3%) than that reported in reference data confirming the occurrence of some chemical and mineralogical inhomogeneity in the various batches of UICC standards. The small amount of Fe^{3+} (0.15 apfu) has been found to be preferentially allocated at $M(1) > M(3)$ suggesting the occurrence of a coupled minor oxo component.

The obtained crystal chemical characterization of the of UICC amosite sample is the basis for further studies in progress aimed at shedding new light on the mechanisms of asbestos-induced toxicity.

REFERENCES

Andreozzi G.B., Ballirano P., Gianfagna A., Mazziotti-Tagliani S., Pacella A., 2009. Structural and spectroscopic characterization of a suite of fibrous amphiboles with high environmental and health relevance from Biancavilla (Sicily, Italy). American Mineralogist 94, 1333-1340.

Andreozzi G.B., Pacella A., Corazzari I., Tomatis M., Turci F., 2017. Surface reactivity of amphibole asbestos: a comparison between crocidolite and tremolite. Scientific Reports 7, 14696.

Ballirano P., 2003. Effects of the choice of different ionization level for scattering curves and correction for small preferred orientation in Rietveld refinement: the $MgAl_2O_4$ test case. Journal of Applied Crystallography 36, 1056-1061.

Ballirano P., Andreozzi G.B., Belardi G., 2008. Crystal chemical and structural characterization of fibrous tremolite from Susa Valley, Italy, with comments on potential harmful effects on human health. American Mineralogist 93, 1349-1355.

Ballirano P., Bloise A., Gualtieri A.F., Lezzerini M., Pacella A., Perchiazzi N., Dogan M., Dogan A.U., 2017. The crystal structure of mineral fibres. In: A.F. Gualtieri (Ed.) "Mineral fibres: crystal chemistry, chemical–physical properties, biological interaction and toxicity". European Mineralogical Union, London, pp. 17-64.

Ballirano P., Celata B., Pacella A., Bosi F., 2021. Recommended X-ray SREF and Rietveld refinement procedure for tremolite. Acta Crystallographica B77, 537-549.

Bancroft G.M., Burns R.G., Maddock A.G., 1967. Determination of cation distribution in the cummingtonite-grunerite series by Mössbauer spectra, American Mineralogist, 52, 1009-1026.

Bernstein D., Dunnigan J., Hesterberg T., Brown R., Velasco J.A.L., Barrera R., Hoskins J., Gibbs A., 2013. Health risk of chrysotile revisited. Critical Reviews in Toxicology 43, 154-183.

Bowes D.R. and Farrow C.M., 1997. Major and trace element compositions of the UICC standard asbestos samples. American Journal of Industrial Medicine 32, 592-594.

Bruker AXS, 2016. Topas V6: General profile and structure

analysis software for powder diffraction data. Bruker AXS, Karlsruhe, Germany.

Cheary R.W. and Coelho A., 1992. A fundamental parameters approach to X-ray line-profile fitting. Journal of Applied Crystallography 25, 109-121.

Chisholm J.E., 1973. Planar defects in fibrous amphiboles. Journal of Materials Science, 8, 475-483.

Delhez R., de Keijser T.H., Langford J.I., Louër D., Mittemeijer E.J., Sonneveld E.J., 1993. Crystal imperfection broadening and peak shape in the Rietveld method: In: Young R.A. (Ed.) "The Rietveld method". Oxford University Press, 132-166.

Dyar M.D., Mackwell S.M., McGuire A.V., Cross, L.R., Robertson, J.D., 1993. Crystal chemistry of Fe^{3+} and H^+ in mantle kaersutite: implications for mantle metasomatism. American Mineralogist, 78, 968-979.

Finger L.W., 1969. The crystal structure and cation distribution of a grunerite. Mineralogical Society of America Special Paper 2, 95-100.

Fubini B., 1993. The possible role of surface chemistry in the toxicity of inhaled fibers. In: Wahreit, D.B. (Ed.), Fiber Toxicology, 11. Academic Press, San Diego, pp. 229-257.

Fubini B., 1996. Physico-chemical and cell free assays to evaluate the potential carcinogenicity of fibres. In: Kane A.B., Boffetta P., Saracci R., Wilbourn J. (Eds.), Mechanisms of Fibre Carcinogenesis. IARC Scientific Publication, Lyon, p. 140.

Garabrant D.H. and Pastula S.T., 2018. A comparison of asbestos fiber potency and elongate mineral particle (EMP) potency for mesothelioma in humans. Toxicology and Applied Pharmacology 361, 127-136.

Gualtieri A.F, Gatta G.D., Arletti R., Artioli G., Ballirano P., Cruciani G., Guagliardi A., Malferrari D., Masciocchi N., Scardi P., 2019. Quantitative phase analysis using the Rietveld method: toward a procedure for checking the reliability and quality of the results. Periodico di Mineralogia 88, 147-151.

Guggenheim S. and Eggleton R.A., 1994. A comparison of the structures and geometric stabilities of stilpnomelane and parsettensite. A distance least-squares (DLS) study. American Mineralogist 79, 438-442.

Hawthorne F.C. and Oberti R., 2007. Amphiboles: Crystal chemistry. In Hawthorne F.C., Oberti R., Della Ventura G., Mottana A. (Eds.), Amphiboles: Crystal chemistry, occurrence, and health issues. Reviews in Mineralogy and Geochemistry, Mineralogical Society of America, Chantilly, Virginia, USA, 67, 1-54.

Hawthorne F.C., Oberti R., Harlow G.E., Maresch W.V., Martin R.F., Schumacher J.C., Welch M.D., 2012. Nomenclature of the amphibole supergroup. American Mineralogist 97, 2031-2048.

Hirschmann M., Ewans W.E., Yang H., 1994. Composition and temperature dependence of Fe-Mg ordering in cummingtonite-grunerite as determined by X-ray diffraction. American Mineralogist 79, 862-877.

Huang S.X., Jaurand M.C., Kamp D.W., Whysner J., Hei T.K., 2011. Role of mutagenicity in asbestos fiber-induced carcinogenicity and other diseases. Journal of toxicology and environmental health Part B, Critical Reviews 14, 179-245.

Hutchison J.L., Irusteta M.C., Whittaker E.J.W., 1975. High-resolution electron microscopy and diffraction studies of fibrous amphiboles. Acta Crystallographica A31, 794-801.

International Agency for Research on Cancer (IARC), 2012. In Arsenic, metals, fibres, and dusts Vol. 100C Monographs on the evaluation of carcinogenic risks to humans, 219-309.

International Ban Asbestos Secretariat http://ibasecretariat.org/alpha_ban_list.php, Revised July 15, 2019 (Accessed 5 May 2020).

Järvinen M., 1993. Application of symmetrized harmonics expansion to correction of the preferred orientation effect. Journal of Applied Crystallography 26, 525-531.

Kamp D.W. and Weitzman S.A., 1999. The molecular basis of asbestos induced lung injury. Thorax 54, 638-52.

Katerinopoulou A., Balic-Zunic T., Lundegaard L.F., 2012. Application of the ellipsoid modeling of the average shape of nanosized crystallites in powder diffraction. Journal of Applied Crystallography 45, 22-27.

Kohyama N., Shinohara Y., Suzuki Y., 1996. Mineral phases and some reexamined characteristics of the International Union against cancer standard asbestos samples. American Journal of Industrial Medicine 30, 515-528.

Le Page Y. and Donnay G., 1976. Refinement of the crystal structure of low-quartz. Acta Crystallographica B32, 2456-2459.

Miyano T. and Beukes N.J., 1997. Mineralogy and petrology of the contact metamorphosed amphibole asbestos-bearing Penge iron formation, Eastern Transvaal, South Africa. Journal of Petrology 5, 651-676.

Mossman B.T. and Churg A., 1998. Mechanisms in the pathogenesis of asbestosis and silicosis. American Journal of Respiratory and Critical Care Medicine 157, 1666-1680.

Mossman B.T., Lippmann M., Hesterberg T.W., Kelsey K.T., Barchowsky A. Bonner J.C., 2011. Pulmonary endpoints (lung carcinomas and asbestosis) following inhalation exposure to asbestos. Journal of Toxicology and Environmental Health Part B, Critical reviews 14, 76-121.

Newbury D.E. and Ritchie N.W., 2013. Is scanning electron microscopy/energy dispersive X-ray spectrometry (SEM/EDS) quantitative? Scanning 35, 141-168.

Oberti R., Cámara F., Della Ventura G., Iezzi G., Benimoff A.I., 2006. Parvo-mangano-edenite and paro-manganotremolite, two new Group 5 monoclinic amphiboles from Fowler, New York, and comments on the solid solution between Ca and Mn^{2+} at the M4 site. American Mineralogist 91, 526-532.

Oberti R., Hawthorne F.C., Cannillo E., Cámara F., 2007. Long-range order in amphiboles. In Hawthorne F.C., Oberti R., Della Ventura G., Mottana A. (Eds.), Amphiboles: Crystal chemistry, occurrence, and health issues. Reviews

in Mineralogy and Geochemistry, Mineralogical Society of America, Chantilly, Virginia, USA, 67, 125-171.

Pacella A., Andreozzi G.B., Ballirano P., Gianfagna A., 2008. Crystal chemical and structural characterization of fibrous tremolite from Ala di Stura (Lanzo Valley, Italy). Periodico di Mineralogia 77, 51-62.

Pacella A., Ballirano P., Cametti G., 2016. Quantitative chemical analysis of erionite fibres using a micro-analytical SEM-EDX method. European Journal of Mineralogy 28, 257-264.

Pacella A., Andreozzi G.B, Nodari L., Ballirano P., 2019. Chemical and structural characterization of UICC crocidolite fibres from Koegas Mine, Northern Cape (South Africa). Periodico di Mineralogia 88, 297-306.

Pacella A., Ballirano P., Fantauzzi M., Rossi A., Nardi E., Capitani G., Arrizza L., Montereali M.R., 2021a. Surface and bulk modifications of amphibole asbestos in mimicked Gamble's solution at acidic pH. Scientific Reports 11, 14249.

Pacella A., Ballirano P., Fantauzzi M., Rossi A., Viti C., Arrizza L., Nardi E., Caprioli R., Montereali M.R., 2021b. Surface and bulk modifications of fibrous erionite in mimicked Gamble's solution at acidic pH. Minerals 11, 914.

Paoletti L., Bruni B.M., Arrizza L., Mazziotti-Tagliani S., Pacella A., 2008. A micro-analytical SEM-EDS method applied to the quantitative chemical compositions of fibrous amphiboles. Periodico di Mineralogia 77, 63-73.

Paoletti L., Bruni B.M., Gianfagna A., Mazziotti-Tagliani S., Pacella A., 2011. Quantitative Energy Dispersive X-ray analysis of sub-micrometric particles using a Scanning Electron Microscope. Microscopy and microanalysis 17, 710-717.

Pollastri S., D'Acapito F., Trapananti A., Colantoni I., Andreozzi G.B., Gualtieri A.F., 2015. The chemical environment of iron in mineral fibres. A combined X-ray absorption and Mössbauer spectroscopic study. Journal of Hazardous Materials 298, 282-293.

Pollastri S., Perchiazzi N., Gigli L., Ferretti P., Cavallo A., Bursi Gandolfi N., Pollok K., Gualtieri A.F., 2017. The crystal structure of mineral fibres. 2. Amosite and fibrous anthophyllite. Periodico di Mineralogia 86, 55-65.

Prescher C., McCammon C., Dubrowinsky L., 2012. MossA: a program for analyzing energy-domain Mössbauer spectra from conventional and synchrotron sources. Journal of Applied Crystallography 45, 329-331.

Ross N.L. and Reeder R.J., 1992. High-pressure structural study of dolomite and ankerite. American Mineralogist 77, 412-421.

Sabine T.M., Hunter B.A., Sabine W.R., Ball C.J., 1998. Analytical expressions for the transmission factor and peak shift in absorbing cylindrical specimens. Journal of Applied Crystallography 31, 47-51.

Sawada H., 1999. Electron density study of garnets: $Z_3Al_2Si_3O_{12}$ (Z=Mg, Fe, Mn, Ca) and $Ca_3Fe_2Si_3O_{12}$. Journal of Solid State Chemistry 142, 273-278.

Shannon R.D., 1976. Revised effective ionic radii and systematic studies of interatomic distances in halides and chalcogenides. Acta Crystallographica A32, 751-767.

Spasiano D. and Pirozzi F., 2017. Treatments of asbestos containing wastes. Journal of Environmental Management 204, 82-91.

Stanton M.F., Layard M., Tegeris A., Miller E., May M., Morgan E., Smith A., 1981. Relation of particle dimension to carcinogenicity in amphibole asbestoses and other fibrous minerals. Journal of the National Cancer Institute 67, 965-975.

Vigliaturo R., Jamnik M., Dražić G., Podobnik M., Tušek Žnidarič M., Della Ventura G., Redhammer G.J., Žnidaršič N., Caserman S., Gieré R., 2022 Nanoscale transformations of amphiboles within human alveolar epithelial cells. Scientific Reports. 12 (1). doi: 10.1038/s41598-022-05802-x.

Vignaroli G., Ballirano P., Belardi G., Rossetti F., 2014. Asbestos fibre identification vs. evaluation of asbestos hazard in ophiolitic rock mélanges, a case study from the Ligurian Alps (Italy). Environmental Earth Sciences 72, 3679-3698.

Whittaker E.J.W., Cressey B.A. and Hutchinson B.L., 1981. Edge dislocations in fibrous grunerite. Mineralogical Magazine 44, 287-291.

Yong T., Dera P., Zhang D., 2019. Single-crystal X-ray diffraction of grunerite up to 25.6 GPa: a new high-pressure clinoamphibole polymorph. Physics and Chemistry of Minerals 46, 215-227.

Young R.A., 1993. Introduction to the Rietveld method: In: Young R.A. (Ed.) "The Rietveld method". Oxford University Press, 1-38.